Nano Energy 134 (2025) 110547

Contents lists available at ScienceDirect

Nano Energy

journal homepage: www.elsevier.com/locate/nanoen

# Supramolecular host-guest complexation creates a "lead cage" for efficient and eco-friendly perovskite solar cells

Qixin Zhuang [a,1], Ke Wang [a,1], Haiyun Li [a], Zhenyu Liu [b], Yanyan Li [c], Yingguo Yang [d], Qianqian Lin [c], Cheng Gong [a], Cong Zhang [a], Zhihao Guo [a], Saif M.H. Qaid [e], Iván Mora-Seró [f], Zhiyuan Xu [a,*], Zhigang Zang [a,*], Huaxin Wang [a,*]

[a] College of Optoelectronic Engineering, Chongqing University, Chongqing 400044, China
[b] CDGM Glass Company Limited, Chengdu, Sichuan, China
[c] Key Lab of Artificial Micro, and Nano-Structures of Ministry of Education of China, School of Physics and Technology, Wuhan University, Wuhan 430072, China
[d] School of Microelectronics, Fudan University, Shanghai 200433, China
[e] Department of Physics & Astronomy, College of Sciences, King Saud University, P.O. Box 2455, Riyadh 11451, Saudi Arabia
[f] Institute of Advanced Materials (INAM), Universitat Jaume I, Castellon 12071, Spain

ARTICLE INFO

*Keywords:*
Perovskite solar cells
Supramolecular
Adsorption
Eco-friendly
Lead leakage

ABSTRACT

Perovskite solar cells' lead toxicity and leakage are key obstacles to commercialization. Here, we introduce a diazapolyoxamacrobicycle structure of cryptand 222 (C222) into the perovskite precursor solution to obtain high-quality films. The abundant diazapolyoxamacrobicycles in C222 can effectively coordinate with $Pb^{2+}$ and form hydrogen bonds with $FA^{+}$ in perovskite, thereby reducing the defect density, suppressing non-radiative recombination, and mitigating lead leakage. As a result, C222-based PSCs achieve a remarkable power conversion efficiency (PCE) of 25.34 % (0.1 $cm^2$) and 23.78 % at a larger area (1.0 $cm^2$), retain over 90 % of its initial PCE after 1500 h of continuous maximum power point tracking (MPPT) under simulated AM 1.5 illumination. Furthermore, the adsorption equilibrium capacity (qe) of C222 is 23.58 mg/g, with an adsorption rate constant ($k_2$) of 0.035 g (mg/min), indicating a lower adsorption potential barrier for anchoring sites, causing an effectively prevention of lead leakage.

## 1. Introduction

Halide perovskite solar cells (PSCs) have garnered considerable interest owing to the cost-effectiveness in manufacturing and rapid increase in power conversion efficiency (PCE)[1,2]. To date, the certified PCE of PSCs has surpassed 26 %, positioning them as robust competitors for the next generation of photovoltaic technology[3–5]. However, it is disheartening that the currently available advanced and efficient PSCs still rely on lead element, inevitably carrying the risk of toxic lead leakage. This risk could pose a serious threat to ecosystem cycles and impact human living environments[6–8], eventually limiting the commercialization of this technology. Therefore, concerted research efforts are needed to control and minimize lead leakage from perovskites in the environment.

The degradation of PSCs mainly results from the less-than-ideal bulk-phase stability of perovskite films under harsh environmental conditions [9]. The low formation energy of perovskite makes it susceptible to the formation of various types of lead-containing deep-level defects on its grain boundaries (GBs) during the anneal process of films (such as uncoordinated $Pb^{2+}$ or $Pb_0$)[10,11]. Deep-level defects typically serve as non-radiative recombination centers for photogenerated charge carriers, significantly diminishing the efficiency and operation stability of the devices. Defects also act as initiators of the degradation process, causing the devices with poor efficiency also preset lower stability[12], and raising the risk of lead leakage[13–15]. As a contingency, recently, extensive research has been devoted to minimizing lead leakage in degrading PSCs by constructing functionalized materials. Researchers have devised strategies for in-situ anchoring $Pb^{2+}$ within perovskite films[16–18]. Specifically, materials with multiple functional groups are introduced into halide perovskites, demonstrating outstanding in-situ Pb anchoring capabilities through strong chemical interactions with $Pb^{2+}$. This can mitigate the issue of lead leakage arising from perovskite

* Corresponding authors.
*E-mail addresses:* zyxu@cqu.edu.cn (Z. Xu), zangzg@cqu.edu.cn (Z. Zang), huaxin.wang@cqu.edu.cn (H. Wang).
[1] The authors contributed equally: Qixin Zhuang, Ke Wang

https://doi.org/10.1016/j.nanoen.2024.110547
Received 27 September 2024; Received in revised form 18 November 2024; Accepted 4 December 2024
Available online 7 December 2024

degradation. Moreover, these embedded functional materials can also minimize defect density, thereby enhancing the photoconversion efficiency (PCE) and the stability of the devices[19–21]. However, considering the intrinsic characteristics of halide perovskites, effectively passivating defects at the source and employing an in-situ anchoring $Pb^{2+}$ strategy within the perovskite films, would be an efficient approach for solving the environmental problems caused by lead leakage.

As cyclic molecules containing ether groups, crown ethers possess highly electronegative cavities that can selectively complex with various metal cations. Consequently, crown ethers are widely employed as complexing agents and phase-transfer catalysts[22,23]. Recent studies have shown that crown ethers, through host-guest interactions with $Pb^{2+}$, can passivate deep-level defects, thereby reducing defect density and optimizing the crystallization of perovskite films. Crown ethers can anchor metal $Pb^{2+}$ in PSCs, thereby mitigating the risk of lead leakage [24]. The interactions between 15-crown-5 and halide perovskite include coordination with metal $Pb^{2+}$ and the formation of hydrogen bonds with $FA^{+}$[25]. On the other hand, 18-crown-6 can stabilize the precursor solution of triple-cation perovskite, facilitate the formation of high-quality films, and prevent moisture erosion[26–29]. Clearly, the supramolecular host-guest complexation between crown ethers and $Pb^{2+}$ is pivotal to improving the performance of PSCs. However, despite significant progress in modifying halide perovskite films with crown ethers, the interaction between most oxygen-containing crown ethers and $Pb^{2+}$ has not been fully satisfactory[30]. Additionally, according to the Gutmann donor number theory[31], crown ethers often exhibit limitations, potentially restricting their ability to passivate defects. Consequently, many PSCs still face the problems of high open circuit voltage ($V_{OC}$) loss and non-optimal long-term operation stability when modified by crown ether.

On the contrary, cryptands easily form coordination complexes with metal cations, such as $Pb^{2+}$ and $K^{+}$, resulting in the formation of double-ring and multi-ring multidentate complexes. In comparison to other coordinating agents, such as crown ethers, cryptands exhibit more stronger coordination ability and more flexible molecular configuration, which makes cryptand show better performance in passivating $Pb^{2+}$-related defect states. Additionally, it is worth noting that the structure of cryptands typically assumes a cage-like form, capable of encapsulating $Pb^{2+}$ within its interior, effectively immobilizing the $Pb^{2+}$ and thus forming a stable complex. This host-guest complexation can prevent the escape and leakage of $Pb^{2+}$ from perovskite materials under harsh environmental conditions. In this study, we innovatively introduce the structure of diazapolyoxamacrobicycles molecule cryptand 222 (referred to as C222) into the halide perovskite precursor solution. It has been discovered that C222 can effectively passivate uncoordinated $Pb^{2+}$ and $Pb_0$ defects, and facilitate the formation of high-quality films, consequently inhibiting non-radiative recombination and enhancing the efficiency and operational stability of the devices. Therefore, C222 modified PSCs achieve an optimized PCE of 25.34 % (0.1 $cm^2$) and 23.78 % at larger area (1.0 $cm^2$) with negligible hysteresis. Moreover, even after 1500 h of continuous maximum power point tracking (MPPT) under simulated AM 1.5 illumination, retains over 90 % of its initial PCE. Furthermore, under damp-heat conditions (85 % RH and 85 °C), the encapsulated device retained 88 % of its initial PCE during 1050 h continuous hours of operation. More importantly, the rich diazapolyoxamacrobicycle structure of C222 can effectively chelate lead ions through host-guest complexation, firmly anchoring lead ions and reducing dramatically lead leakage, thus minimizing the adverse effects of lead on the environment.

## 2. Results and discussion

### 2.1. Chemical interaction between C222 and perovskite components

The diazapolyoxamacrobicycles in C222 can easily form complexes with metal ions, as depicted in Fig. 1**a**. Previous research has indicated that the $Pb^{2+}$ cations in perovskites are coordinated on a plane with two N atoms and four O atoms in the cryptand, forming a highly stable chelate complex that holds promise for reducing the risk of lead leakage [32]. Concurrently, through ion-dipole interactions between the host and guest complexation, C222 can coordinate with $Pb^{2+}$ and form hydrogen bonds with $FA^{+}$ in hybrid halide perovskite films, thus passivating corresponding defects and suppressing non-radiative recombination[33,34]. Hence, drawing from the structural characteristics of C222, we introduce the C222 into the perovskite precursor solution to obtain high-performance and environmentally friendly PSCs. Additionally, to scrutinize the effects on C222 and perovskite, we designated the "Control (without C222)" and "Target (with C222)" samples for subsequent films and devices characterization.

Subsequently, we developed multiple methods for investigating the interaction between C222 and perovskite components, such as the study of chemical changes in the fabricated Control and Target $FA_{0.95}Cs_{0.05}PbI_3$ perovskite films using X-ray photoelectron spectroscopy (XPS). See Supporting Information for further details on film and device fabrication and characterization. Fig. 1**b** depicts two peaks at binding energies of 138.6 eV and 143.5 eV, attributed to Pb 4 $f_{7/2}$ and Pb 4 $f_{5/2}$, respectively. After incorporating C222, both Pb 4 f peaks shift remarkably towards 138.1 eV and 143.0 eV, pointing to an ion-dipole interaction between C222 and perovskite. Additionally, two metal $Pb_0$ signals known as non-radiative recombination centers observed in the control films at 136.6 eV and 141.5 eV cause instability and degradation in device performance[35,36]. The introduction of C222 significantly reduces the metal $Pb_0$ peak, indicating a reduction of sources of non-radiative recombination losses. Moreover, upon the introduction of C222, an O 1 s peak emerges in the Target films in contrast with Control film where this peak is absent, see Fig. 1**c.** Comparing O 1 s peak of the Target films to C222 raw material, it shifts from 532.4 eV to 532.8 eV. This shift suggested chemical interactions between the O in the C222 molecules and the perovskite. Moreover, we also observed that the two peaks associated with Cs $3d_{3/2}$ (737.8 eV) and Cs $3d_{5/2}$ (723.8 eV) in the control films shifted to 737.3 eV and 723.3 eV, respectively, in the Target films, see Fig. S1a. This fact suggests that C222 can also form host-guest interactions with $Cs^{+}$. Furthermore, as present in Fig. S1b, the displacement of the I 3d peak in the Target perovskite films could result from the weakened chemical interaction between Pb and I, possibly stemming from the complexation of C222 with Pb[37]. Similarly, compared to the Control samples, the C-N-C peak shifted toward lower binding energy in the Target films (Fig. S1c), indicating chemical interactions between the N atoms in C222 and the perovskite[38]. Fourier-transform infrared spectroscopy (FTIR) was also utilized to measure C222 raw material, control and target perovskite films. As illustrated in Fig. 1**d** and Fig. S2, the stretching and bending vibration characteristic peaks of the C-O-C ether bond in the C222 raw material at 1124.4 $cm^{-1}$ and 979.5 $cm^{-1}$ shift to lower wavenumbers in the Target perovskite films at 1097.1 $cm^{-1}$ and 950.2 $cm^{-1}$, indicating host-guest complexation between C222 and halide perovskite[39,40]. Furthermore, the stretching vibration peak of the C-N bond is located at 1362.1 $cm^{-1}$, and with the addition of C222, a noticeable shift of the peak to 1352.3 $cm^{-1}$, further indicating the occurrence of ion-dipole interactions between the host and guest. Subsequently, the chemical interaction between perovskite and C222 was analyzed using liquid-state nuclear magnetic resonance spectroscopy (NMR). As depicted in Fig. S3a, it can be observed that in the mixed solution of C222 and $PbI_2$, the shift of each proton peak is very pronounced, indicating strong chemical interactions between C222 and $Pb^{2+}$. Moreover, the chemical shifts of the $NH_2^{+}$ peak in the FAI and C222 mixed solution also indicates the N-H···O hydrogen bonds between C222 and FAI, see Fig. S3b.

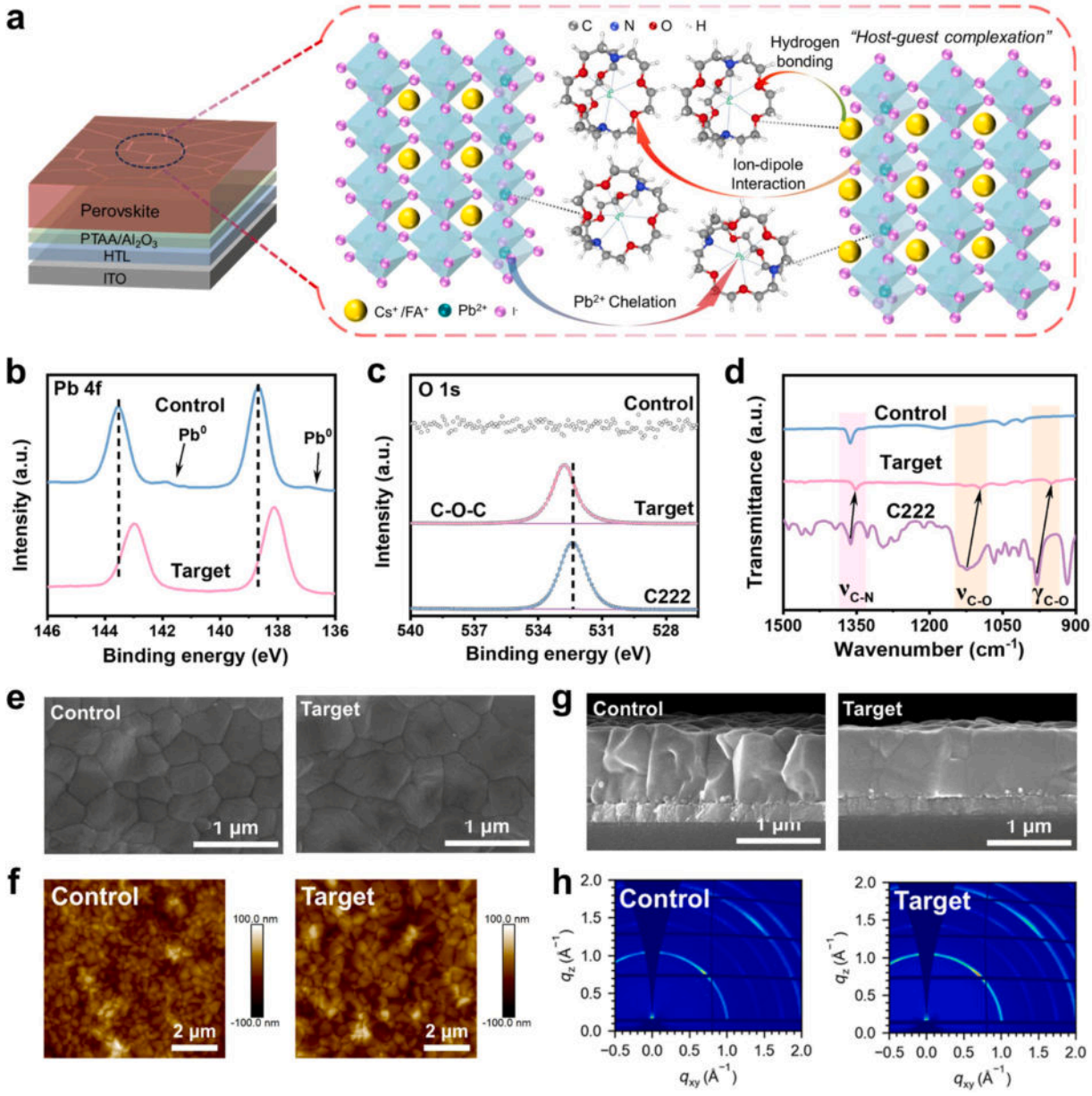


**Fig. 1.** Chemical interaction and morphology.(a) The schematic diagram of the mechanism of C222 regulation in PSCs. XPS spectra of (b) Pb 4 f and (c) O 1 s the C222, Control and Target perovskite films. (d) FTIR spectra of the C222, Control, and Target perovskite films. (e) Surface SEM images of the Control and Target perovskite films. (f) Cross-sectional SEM images of the Control and Target perovskite films. (g) AFM images of the Control and Target perovskite films. (h) GIWAXS images of the Control and Target perovskite films.

### *2.2. Effect of C222 modification on morphology and crystallization of perovskite films*

We utilized scanning electron microscopy (SEM) and atomic force microscopy (AFM) to examine the effects of C222 modification on the morphology of halide perovskite films, as illustrated in high-resolution Fig. 1**e** and low-resolution Fig. S4. It can be obviously observed that the surface morphologies of the perovskite films appear denser and more uniform after C222 modification. Additionally, the grain size increased from 460 nm in the control perovskite films to 553 nm after C222 modification, see Fig. S5, increasing the grain size while decreasing the presence of grain boundaries (GBs). Furthermore, Fig. 1**f** demonstrates that the addition of C222 produces a higher density of grains covering the entire film thickness. Moreover, the perovskite films also achieve a smoother surface after C222 modification, see Fig. 1**g**, the root means square roughness reducing from 20 nm (Control) to 18 nm (Target). Additionally, the increased intensity in XRD diffraction peak and UV absorption, see Fig. S6 and Fig. S7 respectively, also indicate that the Target perovskite films exhibit enhanced crystallinity, which contributed to increased photocurrent density in PSCs[41]. Furthermore, grazing-incidence wide-angle X-ray scattering (GIWAXS) was employed to assess the crystalline quality of perovskite films[42]. At $q$= 1.0 Å$^{-1}$, there were diffraction rings observed in both the control and target samples, corresponding to the perovskite (100) crystal lattice plane, see Fig. 1**h**. Notably, the diffraction peak intensity of the target perovskite films is greater than the control films, indicating that a well-controlled amount of C222 can facilitate generate perovskite films with high crystalline quality. These results collectively suggest that C222 modification contributes to improving halide perovskite film crystalline quality, expecting consequently an impact enhancing photoelectric performance and promoting charge carrier transport, ultimately improving device performance[43].

### 2.3. Effect of C222 modification on carrier dynamics

Subsequently, we examined the effect of the C222 modification on carrier dynamics of perovskites. The steady-state photoluminescence (PL) spectra are presented in Fig. 2**a**. In comparison to the Control perovskite films layered on glass substrates, the C222-modified Target films exhibit increased PL intensity, indicating the reduction of non-radiative recombination, as expected from the enhancement structural properties already commented. Additionally, carrier lifetimes of corresponding perovskite films, see Fig. 2**b**, were assessed via time-resolved photoluminescence spectra (TRPL). TRPL spectra were fitted by a double exponential function equation of $I(t) = I_0 + A_1\exp(-t/\tau_1) + A_2\exp(-t/\tau_2)$, where $A_1$ and $A_2$ represent the decay amplitude of fast and slow decay process, respectively. $\tau_1$ and $\tau_2$ represent the fast and slow decay time constants, respectively. The average carrier lifetime ($\tau_{ave}$) was calculated by using the equation of $\tau_{ave} = (A1\tau_1^2 + A_2\tau_2^2)/(A_1\tau_1 + A_2\tau_2)$. The fitted results reveal a significant extension of the carrier lifetime in the C222-modified films of 597.28 ns compared to that in the control films of 222.19 ns, see Table S1, which is also agreement with the results obtained from PL mapping, see Fig. 2**c**, implying a lower defect density in Target perovskite films[44]. This leads to an increase in carrier lifetime and carrier mobility, pointing to a reduction of trap-assisted non-radiative recombination. Subsequently, we deposited perovskite films on a glass/$NiO_x$/PTAA/$Al_2O_3$ substrate and compared the charge extraction efficiency through the respective PL intensity and fitted TRPL lifetimes, see Figs. 2**d** and 2**e** respectively. The PL intensity decreases for the C222-modified films, and the carrier lifetime decreases from 153.82 ns for the control films to 91.72 ns, see Table S2, indicating that C222 modification significantly improves the charge extraction efficiency, in compliance with the results from PL mapping, see Fig. 2**f**[45]. In summary, C222 modification is poised to accelerate carrier extraction and transport dynamics while suppressing non-radiative recombination processes, thus potentially elevating the photovoltaic efficiency of the devices.

Research has indicated that residual stress is inevitably generated while annealing the halide perovskite films[46]. Consequently, perovskite films were characterized utilizing grazing-incidence X-ray diffraction (GIXRD) to elucidate the stress release effect following the modification of C222. With the grazing incidence angle ($w$) gradually increasing from 0.5° to 1.5°, depicted in Fig. S8a, the diffraction peaks showed a progressive shift towards lower angles in the Control film. In contrast, the Target film exhibited negligible residual stress, see Fig. S8b. Furthermore, the $d$-spacing values of the (001) plane is presented in Fig. S8c. The passivation effect of deep-level defects in perovskite films is crucial for ensuring the stability of the perovskite structure and additionally the release of residual stress[47]. Evidently, the ion-dipole interaction between C222 and uncoordinated $Pb^{2+}$ minimize the defect density, improving the film quality and crystallinity and leading to a significant reduction in residual stress. A decrease in residual stress is expected to contribute to improvements in the PCE and long term stability[42].

### 2.4. Photovoltaic performance of PSCs

Afterward, we utilized a structure of ITO/$NiO_x$/PTAA/$Al_2O_3$/perovskite/PCBM/ BCP/Ag to fabricate the corresponding PSCs. After further optimizing the concentration of C222, the best addition concentration is identified to be 0.3 mg/mL, as highlighted in Fig. S9. Moreover, the detailed statistical photovoltaic performance parameters of 15 devices indicate that the C222-modified devices exhibit significantly improved repeatability, as indicated by the lower standard deviation obtained for Target PSCs, see Fig. S10. The average PCE increased from 22.66 % for the Control devices to 24.79 % for the Target devices, see Fig. 3**a**. The current density-voltage ($J$-$V$) curves of the champion Control and Target device are depicted in Fig. 3**b** and Fig. 3**c**, respectively. Compared to the Control devices, the $V_{OC}$ of the target Devices increased from 1.143 V to 1.180 V, the short-circuit current density ($J_{SC}$) increased from 25.35 mA/cm$^2$ to 25.81 mA/cm$^2$, the fill factor (FF) increased from 80.3 % to 83.2 %, and the PCE also significantly increased from 23.27 % to 25.34 %. As exhibited in Fig. 3**d**, the Target devices achieved a steady-state current density of 24.77 mA/cm$^2$ and a steady-state PCE of 25.25 %, compared to the Control devices (a steady-state current density of 23.49 mA/cm$^2$ and a steady-state PCE of 23.02 %). Furthermore, the incident photon-to-current efficiency (IPCE) spectra, plotted in Fig. 3**e**, indicates that the integral $J_{SC}$ for the Control device is 24.22 mA/cm$^2$, while that for the Target device is 24.62 mA/cm$^2$, with only a 3 % deviation from the $J$-$V$ curve. Finally, for the Target samples, we achieved, for larger-area (1.0 cm$^2$) devices, a PCE as high as 23.78 %, see Fig. 3**f**.

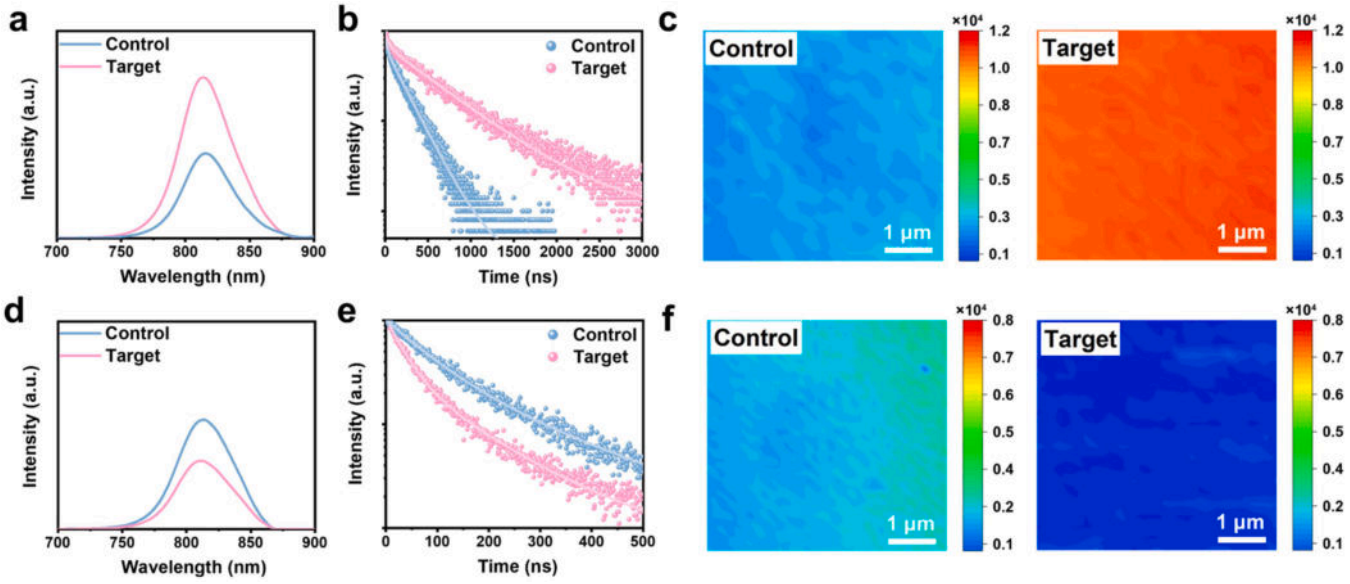


**Fig. 2.** Carrier dynamics. (a) PL spectrum, (b) TRPL curves and (c) PL mapping images of the Control and Target perovskite films layered on glass substrate. (d) PL spectrum, (e) TRPL curves and (f) PL mapping images of the Control and Target perovskite films layered on glass/$NiO_x$/PTAA/$Al_2O_3$ substrate.

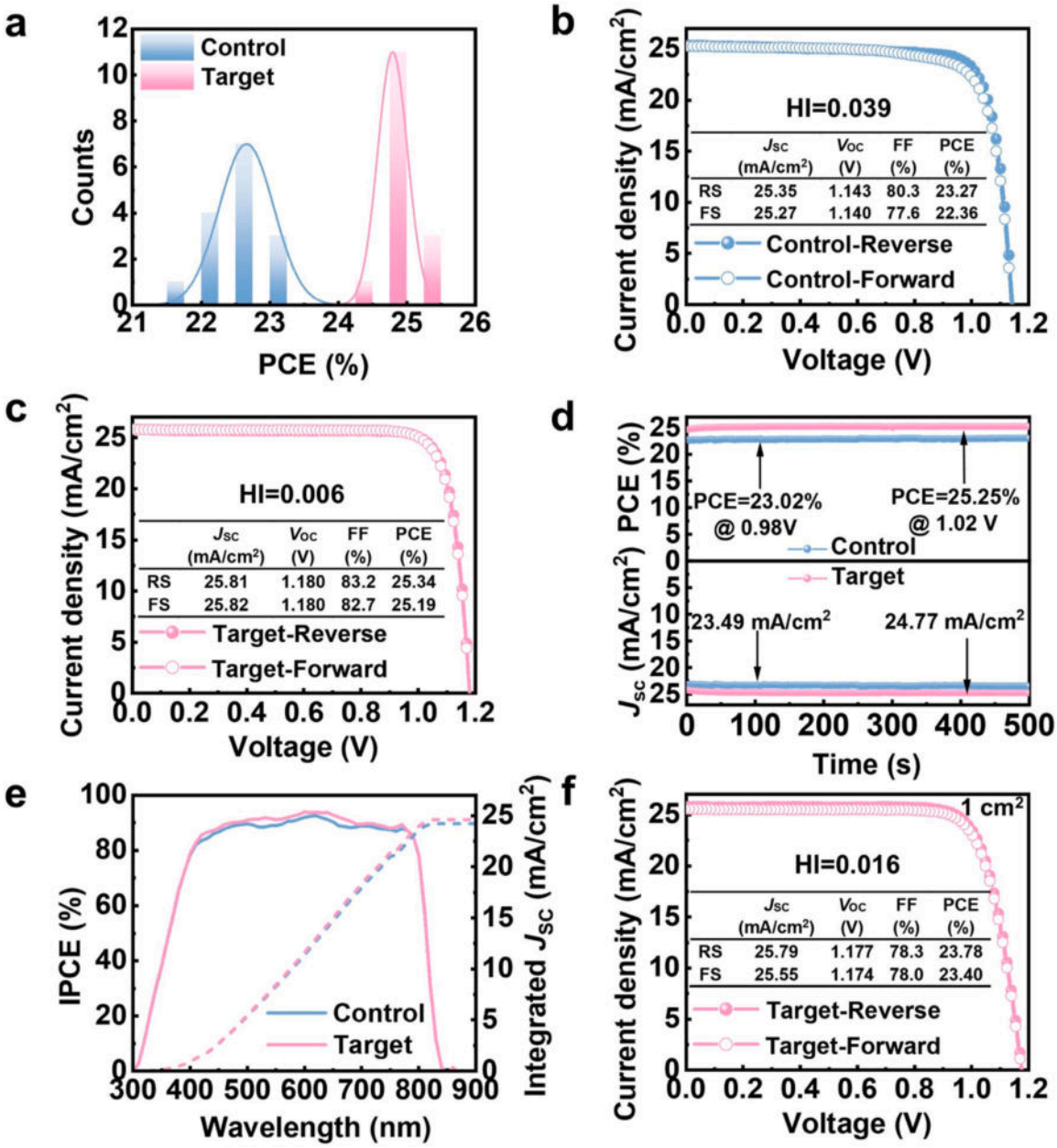


**Fig. 3.** Photovoltaic performance. (a) Statistical distribution diagram of PCE normal square for the control and target PSCs. (b) *J–V* curves of the champion Control and Target PSCs. (d) $J_{SC}$ and PCEs at the MPP tracking for the Control and Target PSCs. (e) IPCE curves and integrated $J_{SC}$ for the Control and Target PSCs. (f) *J–V* curves of the best-performing target device with an active area of 1.0 $cm^2$. Hysteresis index (HI) = $(PCE_{Reverse} - PCE_{Forward})/PCE_{Reverse}$.

### *2.5. Optoelectronic properties of PSCs*

We subsequently conducted further investigations into the electrical characteristics of the PSCs. Transient photocurrent (TPC) measurements were employed to evaluate the carrier extraction and transport efficiency of the devices, see Fig. 4**a**. The TPC decay time was observed to be shorter in the Target devices than in the control devices (0.6 and 1.2 μs, respectively), indicating superior carrier extraction and transfer capabilities[39]. Carrier recombination was assessed through the transient photovoltage (TPV) decay time. As illustrated in Fig. 4**b**, the carrier lifetime of the C222-modified devices increased from 4.6 μs to 14.9 μs, signifying a notable decrease in non-radiative carrier recombination. Furthermore, space charge-limited current (SCLC) measurements were employed to elucidate the density of defect within the perovskite layer. Initially, hole-only devices with and without C222 modification were prepared with an ITO/$NiO_x$/perovskite/Spiro-OMeTAD/Ag structure, while electron-only devices were fabricated with an ITO/$SnO_2$/perovskite/PCBM/Ag structure. Fig. 4**c** reveals that the hole trap density of the Target device significantly decreased from $1.12 \times 10^{16}$ $cm^{-3}$ for the Control device to $3.25 \times 10^{15}$ $cm^{-3}$, Fig. S11, while the electron trap density decreased from $1.35 \times 10^{16}$ $cm^{-3}$ for the Control devices to $3.97 \times 10^{15}$ $cm^{-3}$ after modification, see Fig. S12. This fact indicates that after C222 modification, the halide perovskite material exhibits fewer defect density, providing an improved film quality. Fig. 4**d** depicts the device's Mott-Schottky plot, revealing that the increase in built-in potential ($V_{bi}$) increased from 1.07 V for the Control device to 1.15 V for the Target device. The increased $V_{bi}$ favors an efficient charge injection through the charge transport layers[48]. Subsequently, light intensity-dependent measurements of the *J-V* characteristics were conducted, see Fig. 4**e**. The $V_{OC}$ of the Target device exhibited a linear relationship with the logarithm of light intensity, showing an ideality factor, $n_i$, of 1.27, determined by slope value in $kT/q$ units, which was

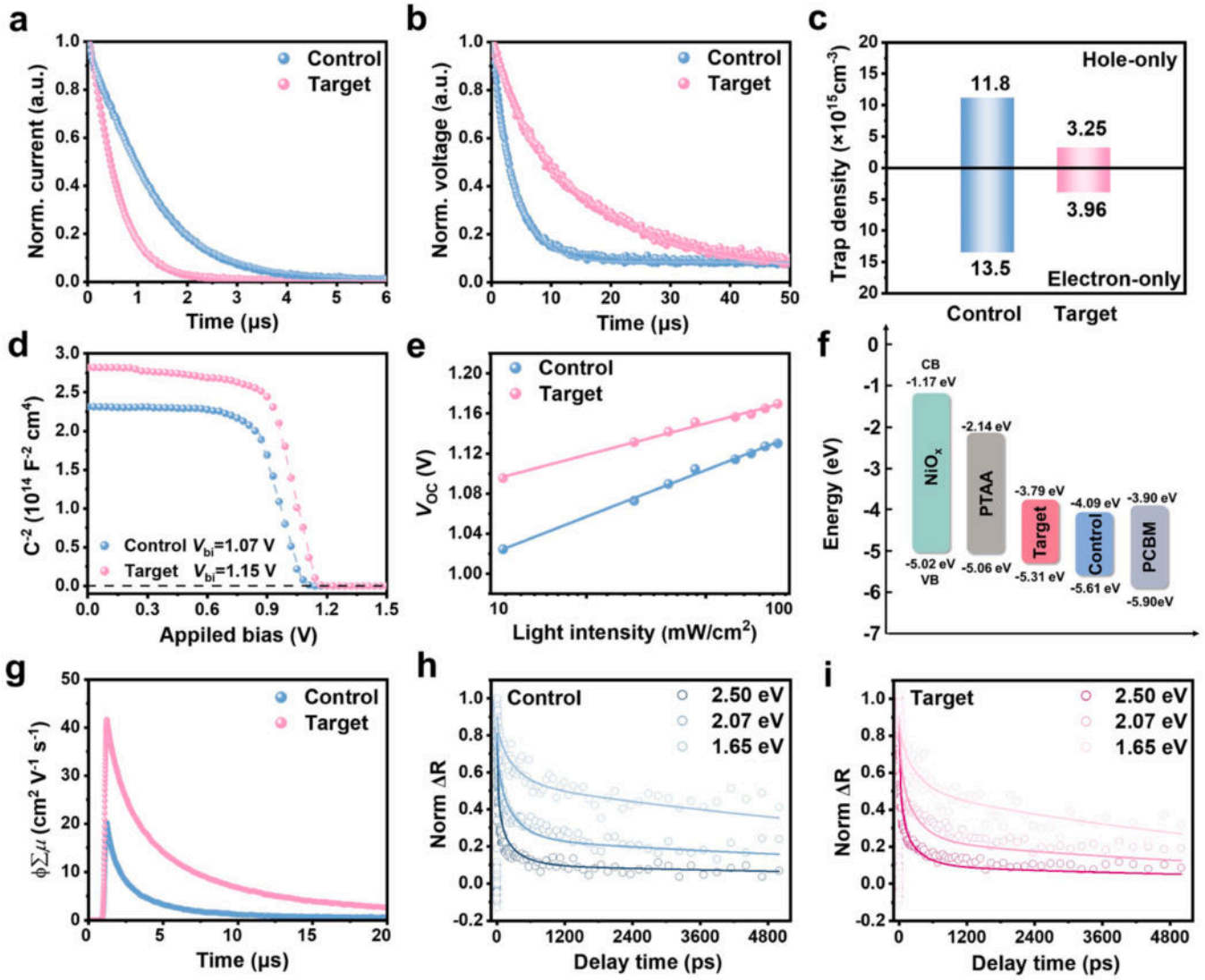


**Fig. 4.** Optoelectronic properties. (a) TPC for the Control and Target PSCs. (b) TPV for the Control and Target PSCs. (c) Calculations and statistics of the trap density for the Control and Target PSCs. (d) M-S curves for the Control and Target PSCs. (e) Light-intensity-dependent $V_{OC}$ of the Control and Target PSCs. (f) Energy level diagram. (g) TRMC curves for the Control and Target perovskite films. (h and i) TRS measurements for the Control and Target perovskite films layered on a glass/$NiO_x$ substance.

markedly lower compared to the Control ideality factor, 1.45 *k*T/q, signifying the reduction of the Shockley-Read-Hall trap mediated non-radiative recombination, leading to enhanced $V_{OC}$ and FF of the device[49]. The ideality factor reduction observed Target devices also indicated an evolution of the recombination mechanism with a higher weight of surface recombination, $n_i = 1$, due to a significant reduction of trap mediated bulk recombination, $n_i = 2$[50].

The alignment of energy levels between the halide perovskite and the charge transport layer is essential for facilitating the extraction and transport of light-generated carriers. We assessed the bandgap and energy levels of C222-modified perovskite films through $T_{auc}$ plots, see Fig. S13, and ultraviolet photoelectron spectroscopy (UPS) measurements. A significant barrier to electron or hole transfer across the interface will hinder charge carrier transport, leading to the recombination of a significant amount of electron-hole pairs at the perovskite/charge transport layer interface and an increase in device $V_{OC}$ loss[51]. As illustrated in Fig. S14 and the corresponding detailed parameter in Table S3, the minimum value of the conduction band of the target perovskite ($E_{CBM}$) shifted from −4.09 eV to −3.79 eV. This shift can diminish the obstacle for electron transfer to the PCBM layer, facilitating electron separation and extraction. Additionally, compared to that of the Control perovskite (-5.61 eV), the Target perovskite's maximum value of the valence band ($E_{VBM}$) (-5.31 eV) is closer to the PTAA layer, promoting hole extraction and transmission. A smaller bandgap offset can lead to higher $V_{OC}$ in PSCs, as depicted in the corresponding energy level diagram in Fig. 4**f**.

Simultaneously, in Fig. 4**g**, the time-resolved microwave conductivity (TRMC) spectra of the perovskite films layered on a glass/$NiO_x$ base are presented. In comparison to the Control film's charge carrier mobility of 20.22 $cm^2\ V^{-1}\ S^{-1}$, the Target perovskite film showed an increased charge carrier mobility of 41.68 $cm^2\ V^{-1}\ S^{-1}$. The diminished defect density and elevated charge carrier transport are likely the primary reasons for the increased charge carrier mobility. Additionally, as illustrated in Fig. S15, the average weighted charge carrier lifetime of the C222-modified devices increases from 3.02 μs to 5.59 μs, see Table S4. Concurrently, we conducted further investigations using transient reflection spectroscopy (TRS) to obtain the surface extraction velocity (SEV)[52,53]. Fig. 4**h** and Fig. 4**i** showcase the surface carrier dynamics measured by transient reflection for three different pump pulse excitations. For the control samples, the extracted SEV is 5660 ± 440 m/s. In contrast, the target samples exhibited an improved SEV (8950 ± 510 m/s). The enhanced hole extraction can be attributed to

improved band alignment, minimized trap density, and increased charge carrier mobility after C222 modification[21,54].

### 2.6. Long-term operation stability of PSCs

Beyond device PCE, an assessment of the stability of both control and target devices was conducted. The long-term operational stability under simulated AM1.5 illumination for continuous maximum power point tracking (MPPT) is showed in Fig. 5**a**. After continuous testing for 1500 h, the target device maintained more than 94 % of its initial PCE at 25.29 %, dramatically higher than the Control device, which declined to 60 % of its initial PCE at 23.20 %. Additionally, following damp-heat aging for the encapsulated devices under 85 % RH and 85 °C conditions. After 1050 h of aging, the target device maintains 88 % of its initial value at 25.03 %, while the control device exhibits a decline in its PCE to the initial 47 % after aging for 750 h, see Fig. 5**b**. These results indicate that the Target devices exhibit superior humidity, light, and thermal stability compared to those of the Control devices, attributed to the improved perovskite film quality with lower defect density as defects act seeds for degradation process.

### 2.7. Pb leakage analysis of PSCs

In addition to performance analysis it is important to remark that the toxicity of lead constitutes a significant impediment to the commercialization of lead-based PSCs[55]. Regarding this consideration, the abundant diazapolyoxamacrobicycles endowed C222 with an outstanding ability to adsorb $Pb^{2+}$, that can also help alleviate this problem. As mentioned above, in comparison to other coordinating agents, such as crown ethers, C222, functioning as a hole-ether material, forms more tightly bound and stronger interactions with $Pb^{2+}$. Consequently, C222 is expected to effectively mitigate the risk of lead leakage by securely anchoring lead within the perovskite layer through conventional chemical interactions thereby mitigating the risk of lead leakage more efficiently. To verify this hypothesis, we conducted simple experiments to confirm the strong host-guest complexation between C222 and $Pb^{2+}$. As shown in Fig. S16a, after adding C222 to the $PbI_2$ precursor solution for 5 min, partial yellow-white substances were observed at the bottom of the bottle. The amount of generated substance increased with prolonged reaction time, and the solution gradually turned slightly yellow, indicating that C222 could adsorb $Pb^{2+}$ in the solution and coordinate with it to form corresponding complexes (C222-Pb). Moreover, unlike the water-soluble $PbI_2$ solution, the generated C222-Pb complexes were insoluble in water and could stably exist in the form of precipitates in water, see Fig. S16b and Fig. S16c. Based on this, we speculate that ether-like molecules with large electronegative cavities have superior ability to adsorb $Pb^{2+}$. Therefore, we further explored the adsorption capacity of C222 and representative crown ether molecules, 15-Crown-5 (15C5), and Dibenzo-21-Crown-7 (DB21C7) for $Pb^{2+}$, and investigated for the first time the adsorption kinetics evolution of these molecules on metal $Pb^{2+}$. Initially, the concentration of $Pb^{2+}$ in the solution was determined via inductively coupled plasma optical emission spectroscopy (ICP-OES). As illustrated in Fig. S17a, compared with that in 15C5 and DB21C7, the concentration of $Pb^{2+}$ in the C222 adsorption solution rapidly decreased with increasing reaction time. This result suggested that C222 adsorbed $Pb^{2+}$ significantly quickly, capturing 72.3 % of the $Pb^{2+}$ in the solution within a mere 5 min. Furthermore, pseudo-first-order and pseudo-second-order kinetic models of the adsorption process are displayed in Fig. S17b and Fig. S17c, respectively. The corresponding curves were fitted, and the fitted results, reported in Table S5 and Table S6, revealed that the pseudo-second-order kinetic model exhibited a higher $R^2$ value. Consequently, we employed this model for the respective adsorption kinetics study. The calculated equilibrium adsorption capacities ($q_e$) during the $Pb^{2+}$ adsorption process of the 15C5, DB21C7 and C222 were found to be 12.50, 14.49, and 23.58 mg/g, respectively. These values closely coincide with the experimental results of $q_e$, which are 11.70, 13.97, and 23.22 mg/g, affirming that the capture of $Pb^{2+}$ by 15C5, DB21C7 and C222[56]. Concurrently, we can calculate the pseudo-second-order adsorption rate constants ($k_2$), where $k_2$-15C5, $k_2$-DB21C7 and $k_2$-C222 are determined to be 0.016, 0.020, and 0.035 g (mg/min), respectively. It is evident that at the same temperature, C222 exhibits the highest $k_2$, indicating a superior adsorption rate for $Pb^{2+}$ and a lower adsorption potential barrier for anchoring sites. This manifestation is attributed to the strong interaction ability of the abundant diazapolyoxamacrobicycles on C222 with $Pb^{2+}$. These results strongly support our hypothesis that C222, which contains abundant diazapolyoxamacrobicycles, can effectively function as a complexing

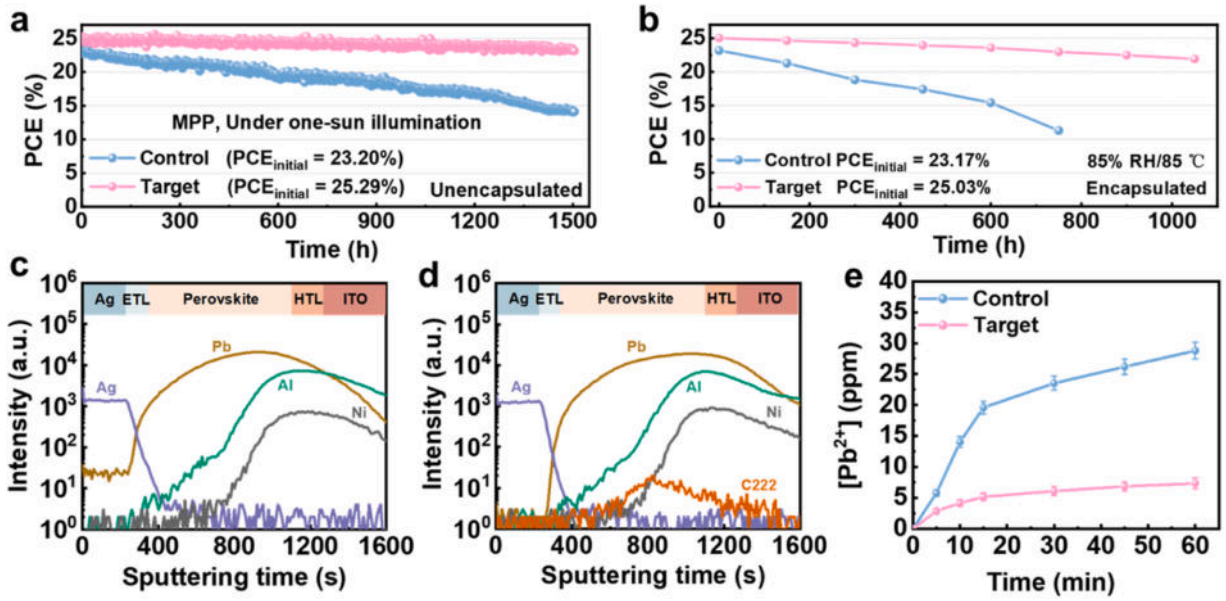


**Fig. 5.** Operation stability and Pb leakage. (a) Stability evolution of unencapsulated Control and Target PSCs measured via MPP tracking under continuous one-sun illumination in $N_2$. (b) Damp-heat stability of the encapsulated Control and Target PSCs kept at 85 % RH and 85 °C in $N_2$. TOF-SIMS analysis of the (c) Control and (d) Target PSCs after aging for 1000 h at 50–60 % RH. (e) Variation in the $Pb^{2+}$ concentration of the Control and Target PSCs immersed in deionized water.

agent for the adsorption of $Pb^{2+}$, thereby preventing lead leakage into the environment.

Additionally, time-of-flight secondary ion mass spectrometry (TOF-SIMS) was employed to assess the escape of $Pb^{2+}$ from PSCs after aging for 1000 h under 50–60 % RH. As presented in Fig. 5**c**, under aging conditions, $Pb^{2+}$ in the Control PSCs move toward the Ag electrode layer through the electron transport layer (ETL), indicating that PSCs are prone to degradation and release lead-containing products into the environment. Encouragingly, for the Target PSCs, almost no $Pb^{2+}$ signals appeared on the Ag electrode layer, see Fig. 5**d**, mainly attributed to the excellent adsorption capability of C222, which effectively anchored lead within the perovskite, thereby mitigating the risk of lead leakage. Further analysis of the concentration of escaped $Pb^{2+}$ in the contaminated water subsequent to the immersion of PSCs can be obtained by examining both Fig. 5**e** and Fig. S18. The amount of $Pb^{2+}$ leakage from PSCs sequentially decreases from the Control to 15C5, DB21C7, and C222 (Target). This suggests that both crown ether and cryptand molecules can mitigate lead leakage, and C222, with its diazapolyoxamacrobicycles, is more effective at capturing $Pb^{2+}$, thereby offering better environmental protection against toxic $Pb^{2+}$. In conclusion, the aforementioned results indicate that the diazapolyoxamacrobicycle groups in C222 play a dominant role in capturing leaked $Pb^{2+}$, contributing to the development of eco-friendly lead-based PSCs. Beyond the implications in Pb sequestration derived from TOF-SIMS analysis, note that C222 is detected in the bulk perovskite film, see Fig. 5**d**, pointing to a preferent location at grain interfaces. This result is also in good agreement with the reduction of trap-mediated bulk recombination indicated by ideality factor reduction in Target devices, see Fig. 4e, as well a defect density reduction, analyzed in Fig. 4**c**.

## 3. Conclusions

In conclusion, for the first time, we report a unique multifunctional supramolecular cryptand material, C222, designed to synergistically mitigate lead-related defects and lead leakage, thereby addressing environmental pollution concerns in PSCs, at the same time that improves PCE and long-term stability. The C222 modification strategy endows halide perovskite films with significant advantages, such as reducing non-radiative recombination, enhancing charge carrier extraction, reducing the defect density, and improving the crystalline quality. Consequently, these outstanding features result in a champion PCE of 25.34 % (0.1 $cm^2$) and 23.78 % (1.0 $cm^2$) with negligible hysteresis for C222-modified PSCs. Furthermore, the C222-based device exhibited excellent operational stability, retain over 90 % and 88 % of its initial PCE after 1500 h of continuous simulated AM 1.5 illumination with MPP tracking and 1050 h of continuous at 85 % RH and 85 °C. More importantly, C222, enriched with abundant diazapolyoxamacrobicycles, C222 chemically anchors and adsorbs toxic $Pb^{2+}$ through host-guest complexation, lowering the risk of lead leakage. This unique supramolecular crown ether material offers an innovative avenue to address the environmental issues associated with potential lead leakage. Therefore, this distinctive supramolecular cryptand material holds wide-ranging applications in the field of perovskite photovoltaics, enabling the development of low-toxicity, environmentally friendly PSCs.

## CRediT authorship contribution statement

**Yanyan Li:** Data curation. **Yingguo Yang:** Data curation. **Iván Mora-Seró:** Writing – review & editing. **Qixin Zhuang:** Writing – original draft, Investigation, Data curation, Conceptualization. **Zhiyuan Xu:** Writing – review & editing, Funding acquisition. **Ke Wang:** Data curation. **Zhigang Zang:** Writing – review & editing, Supervision, Funding acquisition, Conceptualization. **Haiyun Li:** Data curation. **Huaxin Wang:** Writing – review & editing, Funding acquisition. **Zhenyu Liu:** Methodology. **Cheng Gong:** Data curation. **Cong Zhang:** Data curation. **Zhihao Guo:** Data curation. **Saif M. H. Qaid:** Writing – review & editing. **Qianqian Lin:** Data curation.

## Declaration of Competing Interest

The authors declare that they have no known competing financial interests or personal relationships that could have appeared to influence the work reported in this paper.

## Acknowledgements

Q.Z., Z.X., and H.L. contributed equally to this work. This work is funded by the National Natural Science Foundation of China (62204028, 11974063), the Researchers supporting project number (RSPD2024R762), King Saud University, Riyadh, Saudi Arabia; Natural Science Foundation of Chongqing (CSTB2022NSCQ-MSX1514) and China Postdoctoral Science Foundation (2022TQ0391, 2022M710507). The authors would like to thank the Analytical and Testing Center of Chongqing University for various measurements.

### *Author contributions*

Q.Z. and Z.Z conceived the project. Q.Z., K.W., H.L., C.G., C.Z and Z. G prepared the samples and devices. Q.Z. performed all other measurements except for GIWAXS measurements. Y.Y. carried out GIWAXS measurements. Y.L., Z. L., and Q.L. carried out TRMC measurements. Q. Z. wrote the first draft of the manuscript. Q.Z., Z.X., H.W., S.Q., I. M. and Z.Z. wrote the final version of the manuscript. Z.Z. supervised this project. All authors analyzed the data and contributed to the discussions.

## Appendix A. Supporting information

Supplementary data associated with this article can be found in the online version at doi:10.1016/j.nanoen.2024.110547.

## Data availability

The authors do not have permission to share data.

## References

[1] C. Zhang, H. Li, C. Gong, Q. Zhuang, J. Chen, Z. Zang, Crystallization manipulation and holistic defect passivation toward stable and efficient inverted perovskite solar cells, Energy Environ. Sci. 16 (2023) 3825–3836, https://doi.org/10.1039/D3EE00413A.

[2] S.M. Park, M. Wei, J. Xu, H.R. Atapattu, F.T. Eickemeyer, K. Darabi, L. Grater, Y. Yang, C. Liu, S. Teale, et al., Engineering ligand reactivity enables high-temperature operation of stable perovskite solar cells, Science 381 (2023) 209–215, https://doi.org/10.1126/science.adi4107.

[3] NREL (2024). Best research-cell efficiency chart. https://www.nrel.gov/pv/cell-efficiency.html.

[4] H. Li, C. Zhang, C. Gong, D. Zhang, H. Zhang, Q. Zhuang, X. Yu, S. Gong, X. Chen, J. Yang, et al., 2D/3D heterojunction engineering at the buried interface towards high-performance inverted methylammonium-free perovskite solar cells, Nat. Energy 8 (2023) 946–955, https://doi.org/10.1038/s41560-023-01295-8.

[5] Q. Jiang, J. Tong, Y. Xian, R.A. Kerner, S.P. Dunfield, C. Xiao, R.A. Scheidt, D. Kuciauskas, X. Wang, M.P. Hautzinger, et al., Surface reaction for efficient and stable inverted perovskite solar cells, Nature 611 (2022) 278–283, https://doi.org/10.1038/s41586-022-05268-x.

[6] H. Luo, P. Li, J. Ma, L. Han, Y. Zhang, Y. Song, Sustainable Pb management in perovskite solar cells toward eco-friendly development, Adv. Energy Mater. 12 (2022) 2201242, https://doi.org/10.1002/aenm.202201242.

[7] H. Zhang, J.-W. Lee, G. Nasti, R. Handy, A. Abate, M. Grätzel, N.-G. Park, Lead immobilization for environmentally sustainable perovskite solar cells, Nature 617 (2023) 687–695, https://doi.org/10.1038/s41586-023-05938-4.

[8] M. Yang, T. Tian, Y. Fang, W.-G. Li, G. Liu, W. Feng, M. Xu, W.-Q. Wu, Reducing lead toxicity of perovskite solar cells with a built-in supramolecular complex, Nat. Sustain. 6 (2023) 1455–1464, https://doi.org/10.1038/s41893-023-01181-x.

[9] Y. Liang, P. Song, H. Tian, C. Tian, W. Tian, Z. Nan, Y. Cai, P. Yang, C. Sun, J. Chen, et al., Lead leakage preventable fullerene-porphyrin dyad for efficient and stable perovskite solar cells, Adv. Funct. Mater. 32 (2022) 2110139, https://doi.org/10.1002/adfm.202110139.

[10] J. Liang, X. Hu, C. Wang, C. Liang, C. Chen, M. Xiao, J. Li, C. Tao, G. Xing, R. Yu, et al., Origins and influences of metallic lead in perovskite solar cells, Joule 6 (2022) 816–833, https://doi.org/10.1016/j.joule.2022.03.005.
[11] X. Li, W. Zhang, X. Guo, C. Lu, J. Wei, J. Fang, Constructing heterojunctions by surface sulfidation for efficient inverted perovskite solar cells, Science 375 (2022) 434–437, https://doi.org/10.1126/science.abl5676.
[12] N.T.P. Hartono, H. Köbler, P. Graniero, M. Khenkin, R. Schlatmann, C. Ulbrich, A. Abate, Stability follows efficiency based on the analysis of a large perovskite solar cells ageing dataset, Nat. Commun. 14 (2023) 4869, https://doi.org/10.1038/s41467-023-40585-3.
[13] J.-H. Zhao, X. Mu, L. Wang, Z. Fang, X. Zou, J. Cao, Homogeneously large polarons in aromatic passivators improves charge transport between perovskite grains for > 24% efficiency in photovoltaics, Angew. Chem. Int. Ed. 61 (2022) e202116308, https://doi.org/10.1002/anie.202116308.
[14] B. Niu, H. Wu, J. Yin, B. Wang, G. Wu, X. Kong, B. Yan, J. Yao, C.-Z. Li, H. Chen, Mitigating the lead leakage of high-performance perovskite solar cells via in situ polymerized networks, ACS Energy Lett. 6 (2021) 3443–3449, https://doi.org/10.1021/acsenergylett.1c01487.
[15] Q. Cao, T. Wang, J. Yang, Y. Zhang, Y. Li, X. Pu, J. Zhao, H. Chen, X. Li, I. Tojiboyev, et al., Environmental-friendly polymer for efficient and stable inverted perovskite solar cells with mitigating lead leakage, Adv. Funct. Mater. 32 (2022) 2201036, https://doi.org/10.1002/adfm.202201036.
[16] H. Luo, P. Li, J. Ma, X. Li, H. Zhu, Y. Cheng, Q. Li, Q. Xu, Y. Zhang, Y. Song, Bioinspired "cage traps" for closed-loop lead management of perovskite solar cells under real-world contamination assessment, Nat. Commun. 14 (2023) 4730, https://doi.org/10.1038/s41467-023-40421-8.
[17] S. Chen, Y. Deng, X. Xiao, S. Xu, P.N. Rudd, J. Huang, Preventing lead leakage with built-in resin layers for sustainable perovskite solar cells, Nat. Sustain. 4 (2021) 636–643, https://doi.org/10.1038/s41893-021-00701-x.
[18] J. Wang, R. Zhang, H. Xu, Y. Chen, H. Zhang, N.-G. Park, Polyacrylic acid grafted carbon nanotubes for immobilization of lead(ii) in perovskite solar cell, ACS Energy Lett. 7 (2022) 1577–1585, https://doi.org/10.1021/acsenergylett.2c00644.
[19] Y. Zhang, Y. Wang, L. Zhao, X. Yang, C.-H. Hou, J. Wu, R. Su, S. Jia, J.-J. Shyue, D. Luo, et al., Depth-dependent defect manipulation in perovskites for high-performance solar cells, Energy Environ. Sci. 14 (2021) 6526–6535, https://doi.org/10.1039/D1EE02287C.
[20] X. Du, J. Zhang, H. Su, X. Guo, Y. Hu, D. Liu, N. Yuan, J. Ding, L. Gao, S. Liu, Synergistic crystallization and passivation by a single molecular additive for high-performance perovskite solar cells, Adv. Mater. 34 (2022) 2204098, https://doi.org/10.1002/adma.202204098.
[21] C. Gong, X. Chen, J. Zeng, H. Wang, H. Li, Q. Qian, C. Zhang, Q. Zhuang, X. Yu, S. Gong, et al., Functional-group-induced single quantum well dion-jacobson 2d perovskite for efficient and stable inverted perovskite solar cells, Adv. Mater. 36 (2023) 2307422, https://doi.org/10.1002/adma.202307422.
[22] T.-S. Su, F.T. Eickemeyer, M.A. Hope, F. Jahanbakhshi, M. Mladenović, J. Li, Z. Zhou, A. Mishra, J.-H. Yum, D. Ren, et al., Crown ether modulation enables over 23% efficient formamidinium-based perovskite solar cells, J. Am. Chem. Soc. 142 (2020) 19980–19991, https://doi.org/10.1021/jacs.0c08592.
[23] I.V. Kolesnichenko, E.V. Anslyn, Practical applications of supramolecular chemistry, Chem. Soc. Rev. 46 (2017) 2385–2390, https://doi.org/10.1039/C7CS00078B.
[24] P. Gao, Y. Ji, J. Song, G. Zhou, J. Lai, X. Yin, Y. Li, T. Song, Z. Zhao, Q. Chen, et al., Crown ether-induced supramolecular passivation and two-dimensional crystal interlayer formation in perovskite photovoltaics, Cell Rep. Phys. Sci. 2 (2021) 100450, https://doi.org/10.1016/j.xcrp.2021.100450.
[25] K. Chen, Y. Zeng, X. Gao, X. Liu, L. Zhu, F. Wu, Organic semiconductor based on N, S-containing crown ether enabling efficient and stable perovskite solar cells, ChemSusChem 17 (2023) e202301349, https://doi.org/10.1002/cssc.202301349.
[26] R. Chen, Y. Hui, B. Wu, Y. Wang, X. Huang, Z. Xu, P. Ruan, W. Zhang, F. Cheng, W. Zhang, et al., Moisture-tolerant and high-quality α-$CsPbI_3$ films for efficient and stable perovskite solar modules, J. Mater. Chem. A 8 (2020) 9597–9606, https://doi.org/10.1039/D0TA01968B.
[27] X. Wu, Y. Jiang, C. Chen, J. Guo, X. Kong, Y. Feng, S. Wu, X. Gao, X. Lu, Q. Wang, et al., Stable triple cation perovskite precursor for highly efficient perovskite solar cells enabled by interaction with 18c6 stabilizer, Adv. Funct. Mater. 30 (2020) 1908613, https://doi.org/10.1002/adfm.201908613.
[28] R. Chen, Y. Wu, Y. Wang, R. Xu, R. He, Y. Fan, X. Huang, J. Yin, B. Wu, J. Li, N. Zheng, Crown ether-assisted growth and scaling up of $FACsPbI_3$ films for efficient and stable perovskite solar modules, Adv. Funct. Mater. 31 (2021) 2008760, https://doi.org/10.1002/adfm.202008760.
[29] K. Sim, T. Nakao, M. Sasase, S. Iimura, J. Kim, H. Hosono, 18-Crown-6 additive to enhance performance and durability in solution-processed halide perovskite electronics, Small 18 (2022) 2202298, https://doi.org/10.1002/smll.202202298.
[30] P.W. Ayers, R.G. Parr, R.G. Pearson, Elucidating the hard/soft acid/base principle: a perspective based on half-reactions, J. Chem. Phys. 124 (2006) 194107, https://doi.org/10.1063/1.2196882.
[31] V. Gutmann, Empirical parameters for donor and acceptor properties of solvents, Electrochim. Acta 21 (1976) 661–670, https://doi.org/10.1016/0013-4686(76)85034-7.
[32] S. Garcia-Granda, M.R. Diaz, F. Gomez-Beltran, D. Blanco-Gomis, Structure of (4,7,13,16,21,24-hexaoxa-1,10-diazabicyclo[8.8.8]hexacosane)lead(II) eosin dihydrate, Acta Cryst. C. 49 (1993) 884–886, https://doi.org/10.1107/S010827019200979X.
[33] N. Li, S. Tao, Y. Chen, X. Niu, C.K. Onwudinanti, C. Hu, Z. Qiu, Z. Xu, G. Zheng, L. Wang, et al., Cation and anion immobilization through chemical bonding enhancement with fluorides for stable halide perovskite solar cells, Nat. Energy 4 (2019) 408–415, https://doi.org/10.1038/s41560-019-0382-6.
[34] H. Wang, F. Li, P. Wang, R. Sun, W. Ma, M. Chen, W. Miao, D. Liu, T. Wang, Chlorinated fullerene dimers for interfacial engineering toward stable planar perovskite solar cells with 22.3% efficiency, Adv. Energy Mater. 10 (2020) 2000615, https://doi.org/10.1002/aenm.202000615.
[35] D. Bi, C. Yi, J. Luo, J.-D. Décoppet, F. Zhang, Shaik M. Zakeeruddin, X. Li, A. Hagfeldt, M. Grätzel, Polymer-templated nucleation and crystal growth of perovskite films for solar cells with efficiency greater than 21, Nat. Energy 1 (2016) 16142, https://doi.org/10.1038/nenergy.2016.142.
[36] X. Li, X. Wu, B. Li, Z. Cen, Y. Shang, W. Lian, R. Cao, L. Jia, Z. Li, D. Gao, et al., Modulating the deep-level defects and charge extraction for efficient perovskite solar cells with high fill factor over 86, Energy Environ. Sci. 15 (2022) 4813–4822, https://doi.org/10.1039/D2EE02543D.
[37] J.-W. Lee, D.-H. Kim, H.-S. Kim, S.-W. Seo, S.M. Cho, N.-G. Park, Formamidinium and cesium hybridization for photo- and moisture-stable perovskite solar cell, Adv. Energy Mater. 5 (2015) 1501310, https://doi.org/10.1002/aenm.201501310.
[38] X. Sun, F. Deng, S. Li, Y. Li, X. Lv, Y.-Z. Zheng, X. Tao, Dibenzo-18-crown-6-assisted inhibition of cation migration for stable perovskite solar cells, Sol. RRL 6 (2022) 2200303, https://doi.org/10.1002/solr.202200303.
[39] Q. Guo, Z. Dai, C. Dong, Y. Ding, N. Jiang, Z. Wang, L. Gao, C. Duan, Q. Guo, E. Zhou, 17.3% efficiency $CsPbI_2Br$ solar cells by integrating a near-infrared absorbed organic bulk-heterojunction layer, Chem. Eng. J. 461 (2023) 142025, https://doi.org/10.1016/j.cej.2023.142025.
[40] H. Chen, Q. Cheng, H. Liu, S. Cheng, S. Wang, W. Chen, Y. Shen, X. Li, H. Yang, H. Yang, et al., Organic-semiconductor-assisted dielectric screening effect for stable and efficient perovskite solar cells, Sci. Bull. 67 (2022) 1243–1252, https://doi.org/10.1016/j.scib.2022.04.011.
[41] W. Sheng, J. He, J. Yang, Q. Cai, S. Xiao, Y. Zhong, L. Tan, Y. Chen, Multifunctional metal-organic frameworks capsules modulate reactivity of lead iodide toward efficient perovskite solar cells with uv resistance, Adv. Mater. 35 (2023) 2301852, https://doi.org/10.1002/adma.202301852.
[42] J. Tong, J. Gong, M. Hu, S.K. Yadavalli, Z. Dai, F. Zhang, C. Xiao, J. Hao, M. Yang, M.A. Anderson, et al., High-performance methylammonium-free ideal-band-gap perovskite solar cells, Matter 4 (2021) 1365–1376, https://doi.org/10.1016/j.matt.2021.01.003.
[43] Y. Zheng, X. Wu, J. Liang, Z. Zhang, J. Jiang, J. Wang, Y. Huang, C. Tian, L. Wang, Z. Chen, C.-C. Chen, Downward homogenized crystallization for inverted wide-bandgap mixed-halide perovskite solar cells with 21% efficiency and suppressed photo-induced halide segregation, Adv. Funct. Mater. 32 (2022) 2200431, https://doi.org/10.1002/adfm.202200431.
[44] C. Zhang, H. Wang, H. Li, Q. Zhuang, C. Gong, X. Hu, W. Cai, S. Zhao, J. Chen, Z. Zang, Simultaneous passivation of bulk and interface defects through synergistic effect of anion and cation toward efficient and stable planar perovskite solar cells, J. Energy Chem. 63 (2021) 452–460, https://doi.org/10.1016/j.jechem.2021.07.011.
[45] D. Wang, J. Chen, P. Zhu, Y. Qiao, H. Hu, J. Zeng, J. Zhang, G. Qu, Y. Wang, X. Wang, et al., Binary microcrystal additives enabled antisolvent-free perovskite solar cells with high efficiency and stability, Adv. Energy Mater. 13 (2023) 2203649, https://doi.org/10.1002/aenm.202203649.
[46] H. Min, S.-G. Ji, S.I. Seok, Relaxation of externally strained halide perovskite thin layers with neutral ligands, Joule 6 (2022) 2175–2185, https://doi.org/10.1016/j.joule.2022.06.031.
[47] C. Luo, G. Zheng, F. Gao, X. Wang, C. Zhan, X. Gao, Q. Zhao, Engineering the buried interface in perovskite solar cells via lattice-matched electron transport layer, Nat. Photon. 17 (2023) 856–864, https://doi.org/10.1038/s41566-023-01247-4.
[48] O.J. Sandberg, J. Kurpiers, M. Stolterfoht, D. Neher, P. Meredith, S. Shoaee, A. Armin, On the question of the need for a built-in potential in perovskite solar cells, Adv. Mater. Inter. 7 (2020) 2000041, https://doi.org/10.1002/admi.202000041.
[49] Z. Zheng, M. Xia, X. Chen, X. Xiao, J. Gong, J. Liu, J. Du, Y. Tao, Y. Hu, A. Mei, et al., Enhancing the performance of FA-based printable mesoscopic perovskite solar cells via the polymer additive, Adv. Energy Mater. 13 (2023) 2204335, https://doi.org/10.1002/aenm.202204335.
[50] W. Tress, M. Yavari, K. Domanski, P. Yadav, B. Niesen, J.P. Correa Baena, A. Hagfeldt, M. Graetzel, Interpretation and evolution of open-circuit voltage, recombination, ideality factor and subgap defect states during reversible light-soaking and irreversible degradation of perovskite solar cells, Energy Environ. Sci. 11 (2018) 151–165, https://doi.org/10.1039/C7EE02415K.
[51] Y. Wu, B. Chang, L. Wang, H. Li, L. Pan, Z. Liu, L. Yin, Intrinsic dipole arrangement to coordinate energy levels for efficient and stable perovskite solar cells, Adv. Mater. 35 (2023) 2300174, https://doi.org/10.1002/adma.202300174.
[52] X. Chen, H. Lu, K. Wang, Y. Zhai, V. Lunin, P.C. Sercel, M.C. Beard, Tuning spin-polarized lifetime in two-dimensional metal–halide perovskite through exciton binding energy, J. Am. Chem. Soc. 143 (2021) 19438–19445, https://doi.org/10.1021/jacs.1c08514.
[53] J. Xue, R. Wang, X. Chen, C. Yao, X. Jin, K.-L. Wang, W. Huang, T. Huang, Y. Zhao, Y. Zhai, et al., Reconfiguring the band-edge states of photovoltaic perovskites by conjugated organic cations, Science 371 (2021) 636–640, https://doi.org/10.1126/science.abd4860.
[54] Z. Zhu, K. Mao, K. Zhang, W. Peng, J. Zhang, H. Meng, S. Cheng, T. Li, H. Lin, Q. Chen, et al., Correlating the perovskite/polymer multi-mode reactions with

deep-level traps in perovskite solar cells, Joule 6 (2022) 2849–2868, https://doi.org/10.1016/j.joule.2022.10.007.
[55] Y. Gao, Y. Hu, C. Yao, S. Zhang, Recent advances in lead-safe perovskite solar cells, Adv. Funct. Mater. 32 (2022) 2208225, https://doi.org/10.1002/adfm.202208225.
[56] K.S. Kencana, H.J. Choi, K.C. Kemp, S.B. Hong, Enhancing the $CO_2$ adsorption kinetics on Na-RHO and Cs-MER zeolites by $NH_4F/H_2O_2$ etching induced mesoporosity, Chem. Eng. J. 451 (2023) 138520, https://doi.org/10.1016/j.cej.2022.138520.

Qixin Zhuang received his Ph.D. in 2024 under the supervision of Professor Zhigang Zang at the College of Optoelectronic Engineering, Chongqing University. His research focuses on developing high-efficiency and stable perovskite solar cells.

Ke Wang is currently pursuing a Ph.D. under the supervision of Professor Zhigang Zang at the College of Optoelectronic Engineering, Chongqing University. His research primarily focuses on the development of high-efficiency and stable perovskite solar cells.

Zhenyu Liu serves as the General Manager of Chengdu Guangming Optoelectronics and is a senior engineer at the researcher level. He has extensive experience in the field of specialty glass and has led the research, development, and industrialization of various products, including lanthanide rare earth optical glass, fluorophosphate optical glass, and special dispersion optical glass.

Haiyun Li earned his Ph.D. in 2024 under the supervision of Professor Zhigang Zang at the College of Optoelectronic Engineering, Chongqing University. His research primarily focuses on the development of high-efficiency and stable perovskite solar cells.

Yanyan Li earned her Ph.D. in 2023 from Wuhan University and currently serves as a lecturer at Wuhan Textile University. Her research primarily focuses on the development of high-efficiency hybrid organic-inorganic perovskite solar cells and sulfide-based solar cells.

Yingguo Yang is a researcher at Fudan University. His research focuses on new optoelectronic materials, microelectronic devices, semiconductor surface and interface process control, and advanced characterization techniques.

Qianqian Lin is a professor at Wuhan University. His research has been concentrated on crystal growth, optoelectronic devices, transport and recombination properties, photocatalysis, as well as the electrical characterization of photovoltaic.

Cheng Gong earned his Ph.D. in 2024 under the supervision of Professor Zhigang Zang at the College of Optoelectronic Engineering, Chongqing University. His current research focuses on the development of high-efficiency and stable perovskite solar cells.

Cong Zhang earned his Ph.D. in 2023 under the supervision of Professor Zhigang Zang at the College of Optoelectronic Engineering, Chongqing University. His current research focuses on the development of high-efficiency and stable perovskite solar cells.

Zhihao Guo is currently pursuing a Ph.D. under the supervision of Professor Zhigang Zang at the College of Optoelectronic Engineering, Chongqing University. Her research primarily focuses on high-efficiency and stable organic-inorganic hybrid perovskite solar cells.

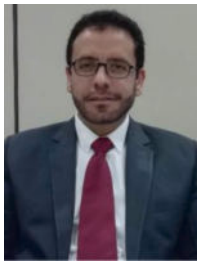

**Saif M. H. Qaid is an associate professor at King Saud University. His research interests primarily include the fabrication and characterization of photonic materials and devices (LEDs, lasers, photovoltaics, detectors, etc.), as well as the field of nanotechnology**.

Iván Mora Seró is a professor at Universitat Jaume I de Castelló. His research focuses on crystal growth, optoelectronic devices, transport and recombination properties, photocatalysis, and the electrical characterization of photovoltaic systems.

Zhiyuan Xu is currently an assistant research fellow under the supervision of Professor Zhigang Zang at the College of Optoelectronic Engineering, Chongqing University. His research focuses on organic-inorganic hybrid perovskite solar cells, flexible electronic and optoelectronic devices, and energy conversion technologies.

Zhigang Zang is currently a full professor in the College of Optoelectronic Engineering at Chongqing University. His research interests include organic and inorganic semiconductor materials and their applications in optoelectronic devices, such as solar cells, LEDs, and detectors.

Huaxin Wang is currently an associate professor at the College of Optoelectronic Engineering at Chongqing University. His research focuses on highly efficient hybrid organic-inorganic perovskite solar cells and inorganic perovskite solar cells.